Advances in Applied Mathematics and Mechanics
Adv. Appl. Math. Mech., Vol. **15**, No. 6, pp. 1379-1406

DOI: 10.4208/aamm.OA-2021-0250
December 2023

Edge Detectors Based on Pauta Criterion with Application to Hybrid Compact-WENO Finite Difference Scheme

Chunhua Zhang[1], Zhen Gao[1], Sa Ye[2] and Peng Li[3,*]

[1] *School of Mathematical Sciences, Ocean University of China, Qingdao, Shandong 266100, China*
[2] *Institute of Agricultural Information, Chinese Academy of Agricultural Sciences, Key Laboratory of Agricultural Big Data, Ministry of Agriculture and Rural Affairs, Beijing 100081, China*
[3] *Department of Engineering Mechanics, Shijiazhuang Tiedao University, Shijiazhuang, Hebei 050043, China*

Received 29 July 2021; Accepted (in revised version) 23 January 2022

Abstract. In the last two decades, many edge detection methods have been developed and widely used in image processing for edge detection and the hybrid compact-WENO finite difference (hybrid) schemes for solving the system of hyperbolic conservation laws with solutions containing both discontinuous and complex fine-scale structures. However, many edge detection methods include the problem-dependent parameters such as the high order multi-resolution (MR) analysis (Harten, JCP, 49 (1983)). Therefore, we combined the Tukey's boxplot method with MR analysis (Gao et al., JSC, 73 (2017)) to overcome this problem in a sense. But the Tukey's boxplot method needs to sort the data at the beginning of Runge-Kutta time integration method, which is relatively time-consuming and inefficient. In this study, we employ the PauTa criterion and remove the problem-dependent parameters in the MR analysis. Furthermore, two new edge detection approaches, which are based on second-order central difference scheme and Ren's idea (Ren et al., JCP, 192 (2003)), are also proposed. The accuracy, efficiency and robustness of the hybrid scheme with the new edge detectors are verified by numerous classical one- and two-dimensional examples in the image processing and compressible Euler equations with discontinuous solutions.

AMS subject classifications: 65M10, 78A48

Key words: Edge detection, Pauta criterion, multi-resolution, hybrid.

*Corresponding author.
Emails: zhangchunhua@stu.ouc.edu.cn (C. Zhang), zhengao@ouc.edu.cn (Z. Gao), yesa@caas.cn (S. Ye), pengli@stdu.edu.cn (P. Li)

1 Introduction

The nonlinear system of hyperbolic conservation laws can be written compactly as

$$\frac{\partial \mathbf{Q}}{\partial t}+\nabla\cdot\mathbf{F}(\mathbf{Q})=0, \tag{1.1}$$

where $\mathbf{Q}$ and $\mathbf{F}(\mathbf{Q})$ represent the conservative variables and fluxes, respectively, together with appropriate initial and boundary conditions in a Cartesian domain. For example, the two-dimensional compressible Euler equation:

$$\frac{\partial \mathbf{Q}}{\partial t}+\frac{\partial \mathbf{F}}{\partial x}+\frac{\partial \mathbf{G}}{\partial y}=0, \tag{1.2}$$

with

$$\mathbf{Q}=(\rho,\rho u,\rho v,E)^T,\quad \mathbf{F}=(\rho u,\rho u^2+P,\rho uv,(E+P)u)^T,\quad \mathbf{G}=(\rho v,\rho uv,\rho v^2+P,(E+P)v)^T,$$

where ρ is density, E is the total energy, $(u,v)^T$ is the velocity vector, $P=(\gamma-1)(E-\frac{1}{2}\rho(u^2+v^2))$ is the pressure and $\gamma=1.4$ is the specific heat ratio of ideal gas. For the nonlinear hyperbolic conservation laws, even if the initial conditions are sufficiently smooth, the solutions will be discontinuous [1, 14, 21, 27] over time. Therefore, the solutions of such nonlinear systems could create both complex fine smooth and large strong gradient flow structures dynamically in space and time.

The hybrid compact-WENO finite difference (hybrid) scheme, based on the high order nonlinear characteristic-wise weighted essentially non-oscillatory (WENO) scheme [1, 14, 27] and the high resolution spectral-like compact scheme, is widely used for capturing shocks and strong gradients accurately and resolving smooth scale structures of solutions of the system of hyperbolic conservation laws [4, 18, 20, 23, 26]. The key issue in any hybrid scheme is to design an accurate, robust, and efficient high order shock detection algorithm that is capable of determining the smoothness of the solution at any given grid point. Moreover, by assuming a discontinuity as an edge of an object in an image, the edge detection methods in image processing can be directly applied as a shock detector in the hybrid scheme. Therefore, in the last two decades, many edge detection methods have been developed for the edge detection and hybrid scheme for solving the system of hyperbolic conservation laws. Costa et al. [4, 5] presented the arbitrary order multi-resolution (MR) analysis of Harten [11] for recognizing non-smooth and smooth stencils. Don et al. [6] designed a conjugate Fourier shock detection algorithm using the conjugate Fourier partial sums and their derivatives to detect discontinuities. In literature [17], Li et al. discussed in detail the detection effect of various low-precision discontinuity detection methods, such as TVB method [3] and KXRCF method [15]. The results show that in the cases of complex structures, these low-order methods do not capture discontinuities accurately. Gao et al. [8] combined the Tukey's boxplot method [29] with the MR analysis to improve the robustness of the shock detection methods, which essentially removes the need of specifying parameter ϵ_{MR}. Wang et al. [34] proposed a shock detection method based on radial basis function (RBF). However, it requires the inverse of the matrix, which results in lower computational efficiency. Yang et al. [38] derived the RBF method of finite difference form (RBF-FD) formula in the Lagrangian form based on radial basis function interpolation, which avoids the complex calculation of matrix inverse and greatly improves the computational effort. In [24], the authors constructed a shock detection method by considering a variation of Harten's idea [10] and consecutive discrete slopes. It is effective in detecting shock waves, but there a significant drawback that the smooth sine waves cannot be interpreted as the smooth functions [39] correctly because the first-order derivatives are usually large for high frequencies and the second-order derivatives are also large at critical points. Zhao et al. used the troubled cell indicator based on the extreme point of approximated polynomial and deigned a new hybrid WENO scheme for hyperbolic conservation laws in [41]. In [2], the authors improved the troubled cell indicator [41], then used it to design the hybrid WENO-AO method. Fu proposed a discontinuity indicator based on the high order TENO paradigm and constructed a hybrid method with TENO scheme for hyperbolic conservation laws [7]. Guo et al. [9] constructed the hybrid schemes which based on the discontinuity indicator using a more straightforward numerical condition. The VF/CF hybrid method has been constructed in [31] for solving Euler equations and the critical regions were identified using a modified Bhagatwala-Lele shock sensor. Using the nonlinear indicator based on the second-order derivative of the concentration, Hu et al. [12] constructed a hybrid first order and WENO scheme for the high-resolution and computationally efficient modeling of pollutant transport.

However, many edge detection algorithms usually require specifying a problem dependent parameter (see Section 2 for details). Vuik et al. [32] used the Tukey's boxplot method [29] to pinpoint the locations of discontinuities by the outlier-detection algorithm, which identifies the corresponding outliers from the coefficients obtained via the troubled-cell indicator algorithm. Based on the analysis of a large number of field data, an outlier monitoring method based on the PauTa criterion is proposed by Li et al. [19], the experimental results showed that the PauTa criterion could effectively detect abnormal points of groundwater in the process of water level monitoring. Compared with the Tukey's boxplot method, the PauTa criterion does not need to sort the data, which can save the computational time. Therefore, we first propose an efficient edge detector based on the PauTa criterion and remove the problem-dependent parameters in the MR analysis. To improve the performance of the PauTa criterion in discriminating the edge locations from other parts, the physical domain is divided into a set of subdomains containing $30\backsim 50$ grid points. Then the PauTa criterion is applied to each subdomain to detect the edges respectively. Due to the sensitivity of PauTa criterion, small perturbation points may be misjudged as the non-smooth grids. For example, a constant function has a small perturbation on a grid point, and then the small perturbation point may be misjudged as a discontinuous point. In order to overcome this problem, we modify the original PauTa criterion by including the global mean of the data set in the definition of fences in each segmented subdomain. The resulted PauTa criterion can further improve the accuracy, efficiency, and robustness of the edge detection methods. Moreover, we design two new edge detection methods to detect the locations of discontinuities. One is based on the second-order central difference scheme, which is similar to the RBF-FD scheme, but intuitively simpler than the RBF-FD scheme. We refer to this method as the C2 method. The other one is an improved method based on Ren's idea in [24], which will be referred to as the IR method. The accuracy of the proposed methods is verified by several one- and two-dimensional examples in the image processing. We further investigate its capability in detecting the shock locations of complex shocked solutions of compressible Euler equations computed by the hybrid scheme.

This paper is organized as follows. The edge detection algorithms of MR analysis, C2 method and IR method are briefly introduced in Section 2. The new edge detection method based on the PauTa criterion are introduced in Section 3. In Section 4, we investigate the capability of the new methods by several one- and two-dimensional examples in the image processing. A large number of classical one- and two-dimensional shocked flow described by the compressible Euler equations are discussed in Section 5. Conclusions are given in Section 6.

2 Edge detection methods

In this section, we introduce three edge detection methods used to detect the edges of images and the locations of large gradients in the flow filed. However, all of these three methods include the problem-dependent parameters. Our goal is to assume the feature point sequence computed by these methods as the normal distribution, and then use the PauTa criterion to detect the locations of edges.

2.1 Multi-resolution analysis

The basic idea of multi-resolution (MR) analysis [11] is to produce a coarser grid of averages of the point values of a function and measure the differences (MR coefficients) d_i between the interpolated values from the sub-grid and the point values themselves. It has been successfully applied to the high order hybrid schemes [4–6].

Given the grid number N_0 and the initial value of grid spacing Δx_0 in the domain [0,1], a set of nested binary grids are considered,

$$G^k=\{x_i^k,\, i=0,\cdots,N_k\},\quad 0\le k\le L<\log_2 N_0, \tag{2.1}$$

where $x_i^k=i\Delta x_k$ with $\Delta x_k=2^k\Delta x_0$, $N_k=2^{-k}N_0$ and the cell averages of function u at x_i^k:

$$\bar{u}_i^k=\frac{1}{\Delta x_k}\int_{x_{i-1}^k}^{x_i^k} u(x)dx. \tag{2.2}$$

Let $\tilde{u}^k_{2i-1}$ be the approximation to $\bar{u}^k_{2i-1}$ by a unique polynomial of degree $n_{MR}=2s$ that interpolates $\bar{u}^k_{i+l}$, $l\leq s$ at x^k_{i+l}.

The approximation error (or multi-resolution coefficients), taking $k=1$ for a single-level MR, $d_i=\bar{u}^0_{2i-1}-\tilde{u}^0_{2i-1}$ at x_i, has the property that if $u(x)$ is a C^{p-1} function, then

$$d_i\approx\begin{cases} [u_i^{(p)}]\Delta x_1^p, & p\leq q,\\ u_i^{(q)}\Delta x_1^q, & p>q, \end{cases} \tag{2.3}$$

where $q=2s+1$ is the order of approximation, $[\cdot]$ and $(\cdot)$ show the jump ($[f_i]=|f_{i+1}-f_i|$) and the derivatives of the function ($f_i^{(p)}=\frac{d^p}{dx^p}f(x_i)$), respectively. The MR coefficient d_i represents how close the data at the finer mesh can be interpolated by the data at the coarser mesh. Therefore, MR coefficients can be used to evaluate the local smoothness of the function at a given point and MR Flag, Flag_i at x_i, can be given as

$$\text{Flag}_i=\begin{cases} 1, & |d_i|>\epsilon_{MR}, & \text{Non-smooth},\\ 0, & \text{otherwise}, & \text{Smooth}, \end{cases} \tag{2.4}$$

where ϵ_{MR} is the MR tolerance and it is a problem-dependent parameter. Inappropriate selection of ϵ_{MR} will lead to the failure of detecting smooth and non-smooth stencils correctly.

2.2 Second-order central difference scheme

A edge detection algorithm based on radial basis functions (RBF) [34] was proposed and successfully applied in the hybrid scheme. However, in the process of computation, we need to take the inverse of the matrix, which takes a lot of time. The complex matrix inversion process was avoided by the RBF-FD scheme [38]. In this study, we use a new approach based on the C2 method to detect the locations of discontinuities, which is similar to the RBF-FD scheme, but intuitively simpler than the RBF-FD scheme.

Three uniform grid points $\{x_{i-1},x_i,x_{i+1}\}$ are considered, where $\Delta x=x_i-x_{i-1}=x_{i+1}-x_i$. Second-order central difference scheme is obtained by expanding both $f(x_{i+1})$ and $f(x_{i-1})$ using Taylor's formula:

$$f_i'=f'(x_i)=\frac{f(x_{i+1})-f(x_{i-1})}{2\Delta x}, \tag{2.5a}$$

$$f_i''=f''(x_i)=\frac{f(x_{i+1})-2f(x_i)+f(x_{i-1})}{(\Delta x)^2}. \tag{2.5b}$$

The key issue in the edge detection method is to increase the difference between discontinuity and smoothness. The edge set E can be defined by using the information of Eqs. (2.5a) and (2.5b)

$$E=\{x_i|d_i=(f_i')^2+(f_i'')^2\geq\xi_1>0,\ x_i\in X,\ i=1,2,\cdots,N\},$$

where ξ_1 is the problem dependent parameter, d_i is used to measure the smoothness of the function at x_i, and X is the set of grid points.

The definition of edge set takes the information of the first- and second-order derivatives into consideration, which can deal with the discontinuity of the first-order derivative, and increase the differences between smooth and discontinuous regions. In this way, smooth and discontinuous regions can be quickly and easily detected.

2.3 Improved indicator based on Ren's idea

Traditional shock sensors [10, 13, 24] also relied on the first- or second-order discrete derivatives of the flow variables. Harten [10] designed a shock detection function aimed at identifying large variations in the slope of the numerical solution. Ren et al. [24] constructed a shock detection method by considering a variation of Harten's idea [10] and consecutive discrete slopes. The corresponding edge indicator is designed as

$$r_i = 1 - \min\left(1, \frac{z_i}{r_c}\right), \tag{2.6}$$

with

$$z_i = \frac{|2(f_{i+1}-f_i)(f_i-f_{i-1})|+\varepsilon}{(f_{i+1}-f_i)^2+(f_i-f_{i-1})^2+\varepsilon}, \tag{2.7}$$

where $\varepsilon = 0.9r_c\xi^2/(1-0.9r_c)$. This method is effective in tracking shocks by giving the suitable threshold parameters ξ and r_c. However, the two parameters are problem-dependent and it is difficult to determine two appropriate parameters at the same time in practical problems. For example, the high frequency smooth sine waves can be incorrectly interpreted as non-smooth functions [39] by this method ($\xi = 10^{-3}$ and $r_c = 0.5$ used in the method). Another disadvantage of Ren's detector is that it is difficult to employ the PauTa criterion introduced in this study to remove the two problem-dependent parameters. Therefore, we modify the edge indicator based on the Ren's idea as follow:

$$\begin{aligned} d_i &= (f_{i+1}-f_i)^2+(f_i-f_{i-1})^2-|2(f_{i+1}-f_i)(f_i-f_{i-1})| \\ &= (|f_{i+1}-f_i|-|f_i-f_{i-1}|)^2 \\ &= \begin{cases} (f'')^2(\Delta x)^4+o(\Delta x)^6, & (f_{i+1}-f_i)(f_i-f_{i-1}) \geq 0, \\ 4(f')^2(\Delta x)^2+o(\Delta x)^4, & (f_{i+1}-f_i)(f_i-f_{i-1}) < 0, \end{cases} \end{aligned} \tag{2.8}$$

where $\Delta x = x_i - x_{i-1}$. Then the edge set E can be defined by using the information of Eq. (2.8)

$$E = \{x_i | d_i \geq \xi_2 > 0,\ x_i \in X,\ i = 1,2,\dots,N\},$$

where the only threshold parameter ξ_2 is related to the problem.

3 Edge detection algorithm based on the PauTa criterion

The threshold parameter plays an important role in the performance of edge detection algorithm. In order to increase the robustness of the algorithm, the idea proposed in [32] is to use the statistical techniques in data analysis. Gao et al. [8] combined the Tukey's boxplot method [29] with the MR analysis [11] to enhance the robustness of the edge detection method by removing the need of specifying threshold parameter ϵ_{MR} and solve the system of hyperbolic conservation laws by the hybrid scheme. However, the Tukey's boxplot method needs to sort the data at the beginning of Runge-Kutta method, which is relatively slow and inefficient, while the PauTa criterion [30] is relatively effective without sorting data, which is often used to detect outliers of data in statistics [19,33,35,37].

We first introduce the normal distribution before introducing the PauTa criterion. The normal distribution is also known as the Gaussian distribution [40], which is the distribution of a continuous random variable with two parameters μ and σ^2. The parameter μ is the mean of the random variable following the normal distribution, σ is the standard deviation and σ^2 is the variance of the random variable. Therefore, the normal distribution is denoted as $N(\mu,\sigma^2)$. The mean value of a normal distribution μ determines its position, and its standard deviation σ determines the magnitude of the distribution. It can be seen from Fig. 1 that the curve is a bell shaped, so it is often called a bell shaped curve. The PauTa criterion's main idea is as follows:

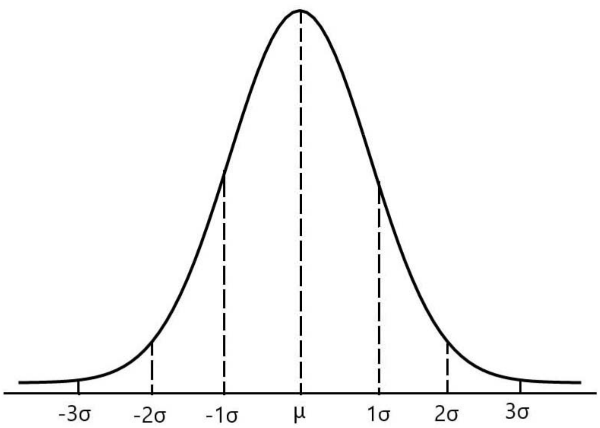

Figure 1: The Normal distribution curve.

PauTa criterion: It is assumed that a set of test data contain only random errors, and standard deviations are obtained through calculation. An interval is determined according to a certain probability. It is believed that any error exceeding this interval is not a random error but a gross error, and the data containing such errors should be eliminated.

This discriminate processing principle is only limited to the normal or approximately normal distribution of the sample data processing. The numerical distribution interval

Table 1: The PauTa criterion.

Numerical distribution interval	The proportion of the data
$(\mu-\sigma,\mu+\sigma)$	0.6827
$(\mu-2\sigma,\mu+2\sigma)$	0.9545
$(\mu-3\sigma,\mu+3\sigma)$	0.9973

and the proportion of the data are shown in Table 1. Compared with the Tukey's boxplot, the edge detection algorithm based on the PauTa criterion has the advantage that it is not necessary to spend time in sorting the data. The main feature is that if most of the data is well distributed (containing only a small number of outliers), it can detect outliers very accurately. Another important feature is that it does not need to specify the number and range of outliers in advance. Furthermore, we assume that there are few discontinuities and shock waves in the numerical solution of system of hyperbolic conservation laws. From the point of view of feature point series computed by the shock detection methods, since the feature values are small in the smooth region while is large in the discontinuous region, the data is approximately normal distribution, so the discontinuous points are similar to the outliers. Therefore, the PauTa criterion can remove the threshold parameter to enhance the robustness of the edge detection algorithm.

A data set is assumed to be as $\mathbf{d}=(d_1,d_2,\cdots,d_N)$. Because the global region may contain complex solution structure (including strong discontinuity, weak discontinuity and fine scales structures), therefore the data points maybe too complex to discriminate the discontinuities from the smooth parts. In this paper, it is recommended that the full physical domain be segmented into n subdomains, each of which contains m data. The data of the jth subdomain is $\mathbf{d}^j=(d_1^j,d_2^j,\cdots,d_m^j)$. The mean of the jth subdomain is called

$$M^j=\frac{1}{m}\Big(\sum_{i=1}^m |d_i^j|\Big).$$

The standard deviation of the jth subdomain is

$$S^j=\sqrt{\sum_{i=1}^m \frac{(d_i^j-M^j)^2}{m}}.$$

To identify the potential outlier(s) in the data set $\mathbf{d}^j$, we give fences $F_1^j=M^j-\alpha S^j$ and $F_2^j=M^j+\alpha S^j$. Using the fences, the domain can be defined as $\Omega_j=[F_1^j,F_2^j]$. Any data d_i^j that lies outside Ω_j ($d_i^j\notin\Omega_j$) is considered to be an outlier and assumed to be the non-smooth Flag at its corresponding grid point that is, $\text{Flag}_i^j=1$. Otherwise, we set $\text{Flag}_i^j=0$. The choice of $\alpha=3$ is commonly used in many literatures such as [19], sometimes $\alpha=2$ can also be selected.

Due to the sensitivity of PauTa criterion, small perturbation points may be misjudged as the outliers and marked as the non-smooth stencils. For example, one can consider the following test function $f(x)$:

$$f(x)=\begin{cases} 5, & -1.5\leq x\leq -1, \\ 0, & -1<x\leq -\dfrac{\pi}{64}, \\ 0.05\sin(256x), & -\dfrac{\pi}{64}<x\leq \dfrac{\pi}{64}, \\ 0, & \dfrac{\pi}{64}<x\leq 1.5, \\ 7, & 1.5<x\leq 2. \end{cases} \tag{3.1}$$

In the left of Fig. 2, the blue line scale represents the MR coefficients, which are approximately normal distribution. The black square shows the locations of discontinuity detected by combining the MR coefficients with original PauTa criterion. It is observed that when a constant function has the small perturbations, the small perturbations are misjudged as discontinuous points. In order to remove false identification of smooth stencils as the non-smooth stencils, we modify the definition of the fences to be

$$F_1^j=\min\{M^j-\alpha S^j,-M\} \quad \text{and} \quad F_2^j=\max\{M^j+\alpha S^j,M\},$$

where

$$M=\frac{1}{N}\Big(\sum_{i=1}^{N}|d_i|\Big) \quad \text{and} \quad N=n\times m.$$

As we can seen from the right of Fig. 2, after including the global mean in the definition of fences in each segmented subdomain, all discontinuities are correctly identified and there is no false identification of smooth stencils as non-smooth stencils.

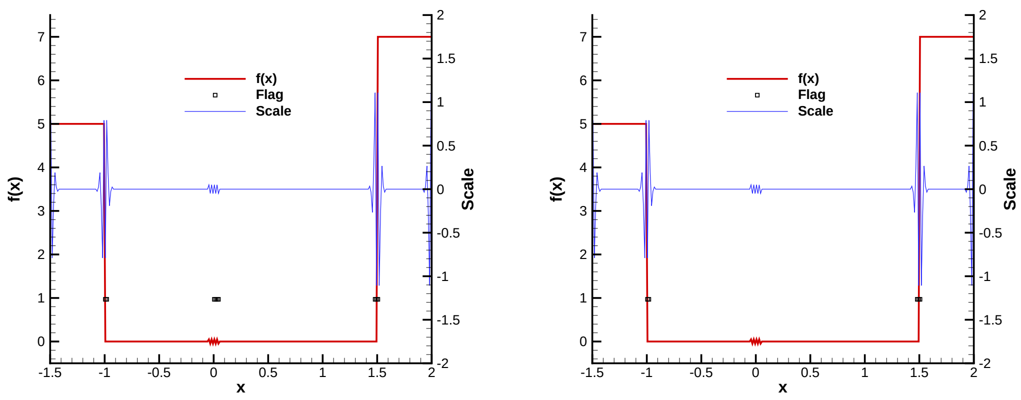

(a) (b)

Figure 2: The non-smooth stencils of $f(x)$ identified by the (a) original and (b) modified PauTa criterion with mesh resolution $N=280$.

Remark 3.1. By testing many numerical examples, we find that the proposed methods can detect the edges accurately when $m\in[30,50]$. For the sake of simplicity, we use $m=40$ in this paper. In the two-dimensional problems, the one-dimensional algorithm is applied in the x- and y-directions respectively. The means M^j, M in the x- and y-directions are computed separately, to obtain M_x^j, M_x and M_y^j, M_y. In addition, we set $\alpha=2$ for the MRS method and $\alpha=3$ for the C2/IR method in our study.

As the end of this section, we summarize the shock detection algorithm based on the PauTa criterion in the following Algorithm 3.1.

Algorithm 3.1 The edge detection algorithm based on the PauTa criterion.

1: Divide the whole physical domain into n uniform subdomains, the data of the jth subdomain is marked as $\mathbf{d}^j=(d_1^j,d_2^j,\cdots,d_m^j)$, $(j=1,\cdots,n)$, where m is the number of grid points in each subdomain.

2: Compute the mean of jth subdomain

$$M^j=\Big(\sum_{i=1}^{m}|d_i^j|\Big)\Big/m, \tag{3.2}$$

and the standard deviation of the jth subdomain

$$S^j=\sqrt{\sum_{i=1}^{m}(d_i^j-M^j)^2/m}. \tag{3.3}$$

3: Compute the modified fences for jth subdomain

$$F_1^j=\min\{M^j-\alpha S^j,-M\} \quad \text{and} \quad F_2^j=\max\{M^j+\alpha S^j,M\}, \tag{3.4}$$

where $M=(\sum_{i=1}^{N}|d_i|)/N$, $\alpha=2$ for MRS method and $\alpha=3$ for C2/IR method.

4: By defining $\Omega_j=[F_1^j,F_2^j]$ on the jth subdomain, the non-smooth/smooth Flag at each grid point in the subdomain will be decided accordingly as

$$\text{Flag}_i^j=\begin{cases} 1, & d_i^j\in\Omega_j, \quad \text{non-smooth stencil},\\ 0, & \text{others}, \quad \text{smooth stencil}. \end{cases} \tag{3.5}$$

4 Numerical results for edge detection

In this section, we will present some one- and two-dimensional examples in the image processing to illustrate the performance of the capability of MR analysis, MR analysis with Tukey's boxplot method (MRQ), MR analysis with PauTa criterion (MRS), C2 with PauTa criterion and IR with PauTa criterion in the image edge detection. The edge set E contains all the centers which are identified as the edges/boundaries/sharp gradients, which means $E=\{x_i|\text{Flag}(x_i)=\text{Flag}_i=1, \forall i\}$.

4.1 One-dimensional piecewise function

Consider the piecewise function $g(x)$:

$$g(x)=\begin{cases} -3, & 0\le x\le 1,\\ 2, & 1<x\le 2.3,\\ 6, & 2.3<x\le 3.8,\\ -1, & 3.8<x\le 5,\\ 8, & 5<x\le 2\pi,\\ 3\sin(15x), & 2\pi<x\le 12. \end{cases} \tag{4.1}$$

Fig. 3 shows the results of the five detection methods. It can be observed that the smooth sine function is misjudged by the MR analysis with the MR tolerance $\epsilon_{MR}=1\times 10^{-1}$ under the low mesh resolution $N=200$. However, the MRQ, MRS, C2 and IR methods can accurately identify the discontinuous region accurately, but MRQ method needs more grid points to resolve a discontinuity. With the mesh resolution $N=400$, the MR analysis and MRQ method reach the similar detection results while the MRS, C2 and IR methods accurately identify the discontinuity region with fewer grid points around the discontinuity.

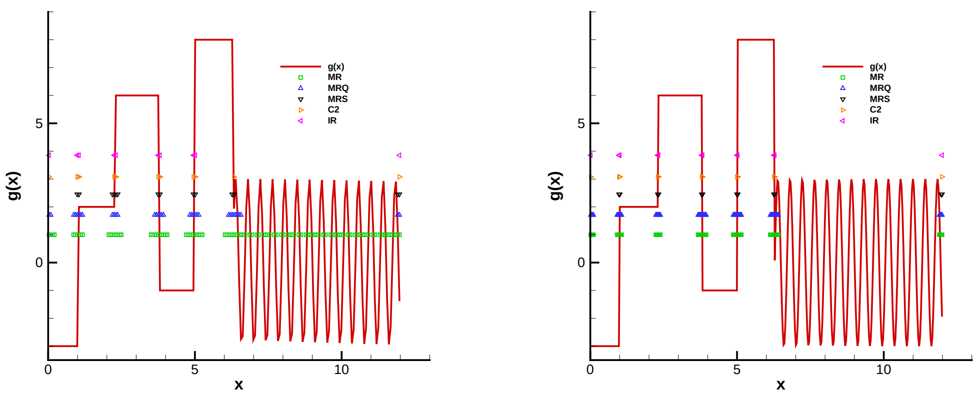

(a) (b)

Figure 3: Discontinuity detection of the piecewise function by the five methods with (a) $N=200$ and (b) $N=400$.

4.2 One-dimensional multi-wave function

We consider a multi-wave function, which includes the smooth Gauss function, discontinuous square function, piecewise linear triangular function and continuous elliptic function. This function is a good example to test the ability of the discontinuity detection methods in identifying the smoothness, discontinuities and first derivative of the function with different mesh resolutions. The function is given as follows:

$$h(x)=\begin{cases} \frac{1}{6}[G(x,\beta,z-\delta)+4G(x,\beta,z)+G(x,\beta,z+\delta)], & x\in[-0.8,-0.6],\\ 1, & x\in[-0.4,-0.2],\\ 1-|10(x-0.1)|, & x\in[0,0.2],\\ \frac{1}{6}[F(x,\alpha,a-\delta)+4F(x,\alpha,a)+F(x,\alpha,a+\delta)], & x\in[0.4,0.6],\\ 0, & \text{else},\end{cases} \tag{4.2}$$

where

$$G(x,\beta,z)=e^{-\beta(x-z)^2},\quad F(x,\alpha,a)=\sqrt{\max(1-\alpha^2(x-a)^2,0)},$$
$$z=-0.7,\quad \delta=0.005,\quad \beta=\frac{\log 2}{36\delta^2},\quad a=0.5,\quad \alpha=10.$$

Fig. 4 shows the detection results, the jump locations in the function at $x=-0.4$ and $x=-0.2$ are accurately determined by the MR analysis with $\epsilon_{MR}=2\times10^{-2}$, but the MR analysis cannot identify the jumps in the first derivative. The MRQ method and MRS method perform better than the MR analysis and can capture the jump in the first derivative at $x=0.1$. The locations of all the discontinuities (both in the jumps in the function

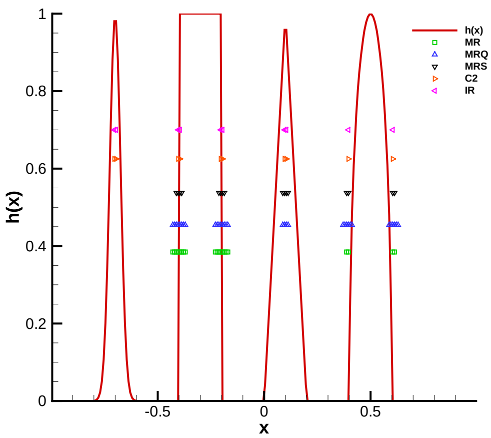

Figure 4: Discontinuity detection of the multi-wave function by the five methods with mesh resolution $N=240$.

and its first derivative) of the multi-wave function are identified more clearly, accurately and sharply by the C2 and IR methods. The results show that the C2 and IR methods can not only capture each discontinuity, but also only with a fewer grid points around it.

4.3 Edge detection of two-dimensional image

In the two-dimensional image detection, the final edge is the union of detection results in the x- and y-directions. Let's consider the Shepp-Logan image, which is used to simulate the gray image of human brain. It consists of a large ellipse (representing the brain with a relatively large function value) and several smaller ellipses (representing some characteristic structures of the brain with a relatively small function value). It is often used to test the ability of edge detection methods to catch small edges with multi-scale discontinuities.

The image mesh resolution is $N\times M = 256\times 256$. Fig. 5 shows the detection results obtained by the five methods. It is clearly observed that the C2 and IR methods can capture the large edges and small discontinuities accurately.

The results of Shepp-Logan image edge detection along the x-direction at $y=170$ is presented in Fig. 6. It shows that the MR analysis with $\epsilon_{MR}=5\times 10^{-5}$ and MRQ method

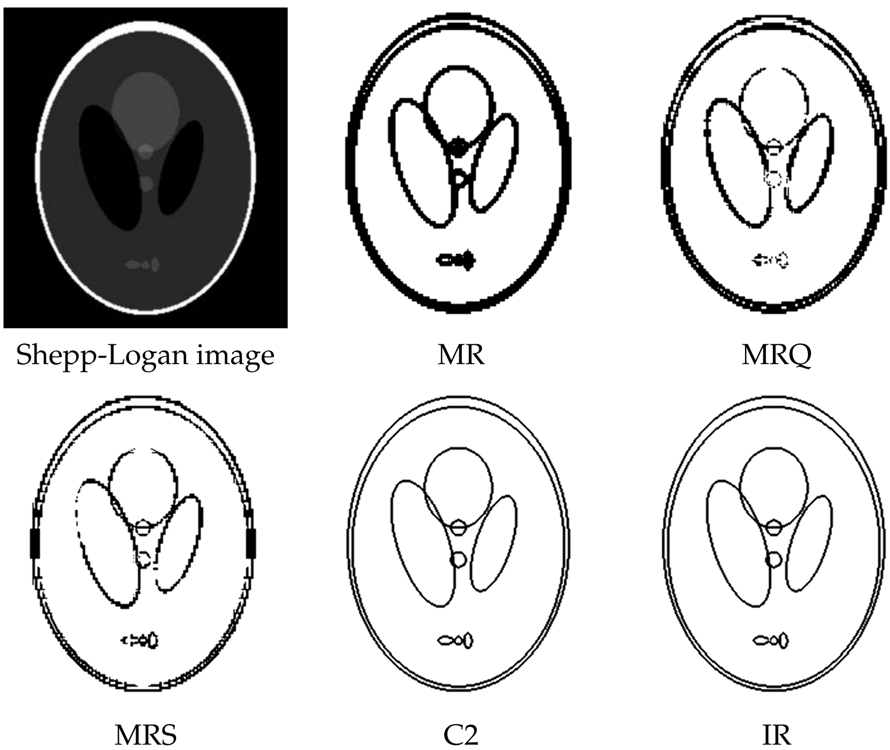

Figure 5: Edge detection results of Shepp-Logan image.

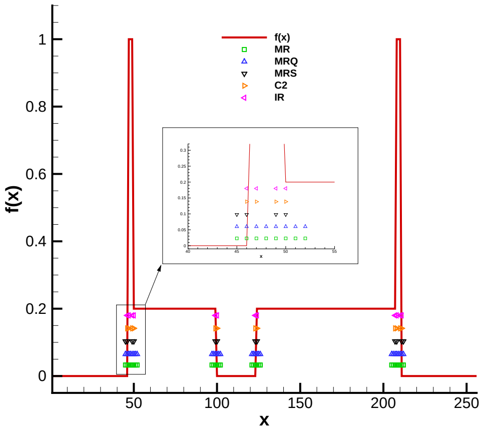

Figure 6: Detection results of Shepp-Logan image with the image resolution $N\times M=256\times 256$ along the x-direction at $y=170$.

can catch the edge accurately, but they need more grid points to detect a discontinuity. The edge detection method based on the MRS, C2 and IR methods can not only accurately detect the edge of discontinuities with different jump sizes, but also only need two grid points to capture a discontinuity. The result shows that the three new methods are superior to the MR analysis and MRQ method in identifying the edge positions.

Fig. 7 shows the edge detection results of a simple image and other three classical images by the five methods with the resolution $N\times M=256\times 256$. It is easy to observe that although some images contain noise and very small discontinuities, the three new methods show good accuracy in detecting strong discontinuities and very small structures.

5 Numerical results for the hybrid schemes

The hybrid scheme in this study conjugates sixth-order central compact finite difference scheme with fifth-order WENO-Z scheme as the framework in [4,6]. For clarity, we show the hybrid compact-WENO scheme in the following Algorithm 5.1 and Fig. 8. The details of the sixth-order compact finite difference scheme and the fifth-order characteristic-wise WENO-Z finite difference scheme with the global Lax-Friedrichs flux splitting via the Roe eigensystem used in this study can be found in [1,16] and will be briefly introduced in Appendix. After spatial discretization, the resulting ordinary differential equations are advanced by the third-order TVD Runge-Kutta time integration method [27]. The CFL number is taken as 0.45.

Remark 5.1. In this study, the derivatives f_0' and f_N' in (A.3) at the left and right compact stencil boundaries are computed by the WENO scheme. This boundary treatment

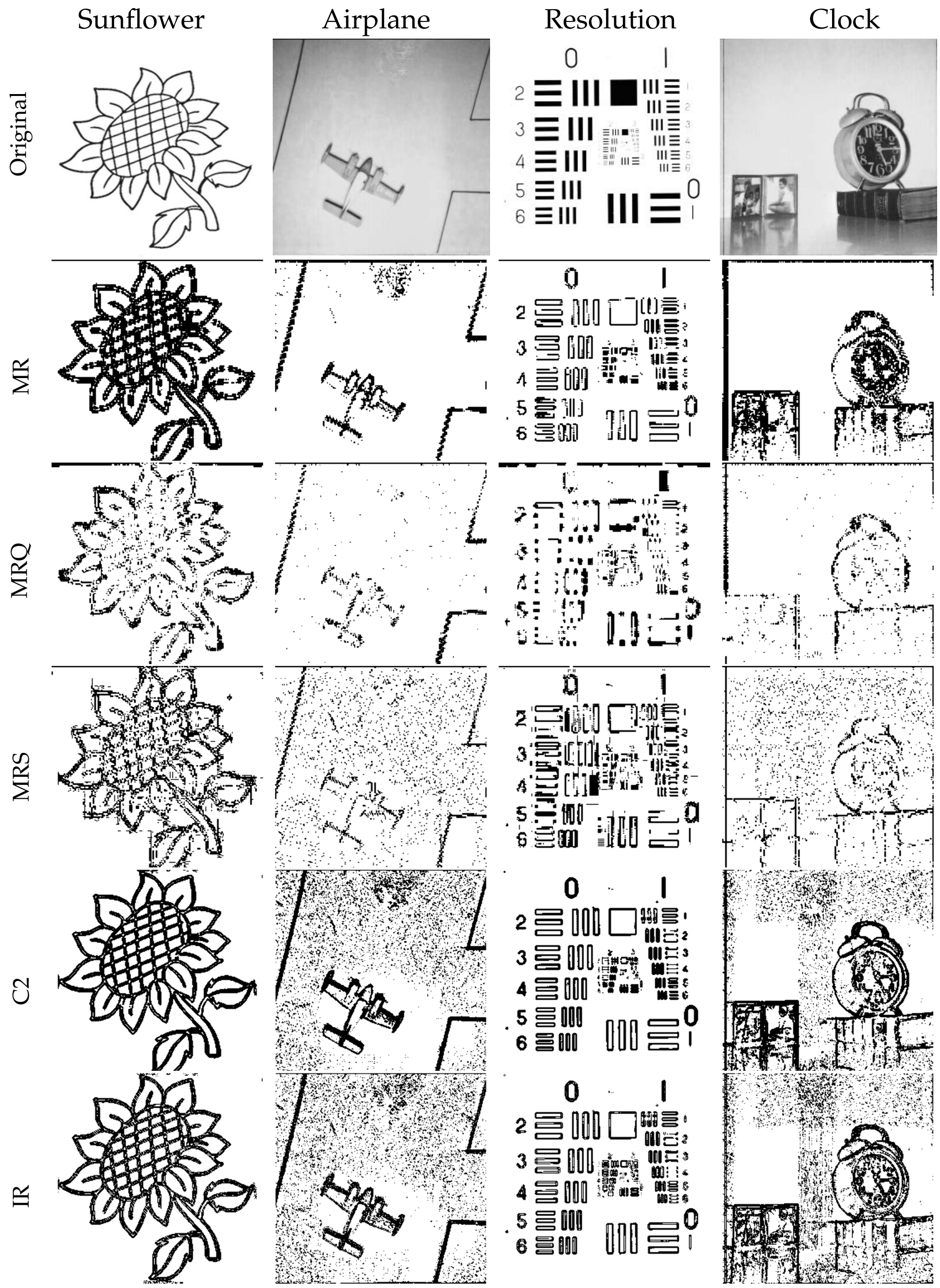

Figure 7: Edge detection results of classical images (256×256). The first line is the original images, which from left to right are Sunflower, Airplane, Resolution and Clock. The second to sixth lines are the image edges detected by MR, MRQ, MRS, C2 and IR methods.

Algorithm 5.1 Hybrid compact-WENO scheme.

1: Determine the smoothness of solution at the given grid points by a shock detect Algorithm 3.1 for one or more suitable variable(s) (typically, density ρ) at the beginning of the Runge-Kutta time step.
2: The grid points which is marked as the non-smooth Flag in Algorithm 3.1 will be set as the non-smooth grid points in the hybrid scheme.
3: Create a buffer zone (blue circle in Fig. 8) around the non-smooth grid point x_i such that all the grid points inside the buffer zone are flagged as the non-smooth stencils. This technique prevents that the derivatives of the fluxes are computed by the compact scheme at the non-smooth grid points.
4: Compute the derivative of the fluxes at each cell center by

- non-smooth stencil (Flag$=$1): the WENO scheme.
- smooth stencil (Flag$=$0): the Compact scheme.

method will destroy the conservation of compact scheme [16], and as a result, the hybrid compact-WENO scheme is not conservative. However, extensive numerical experiences included the numerical examples in this study shows that the proposed hybrid scheme is effective for solving the system of hyperbolic conservation laws [5,8,38].

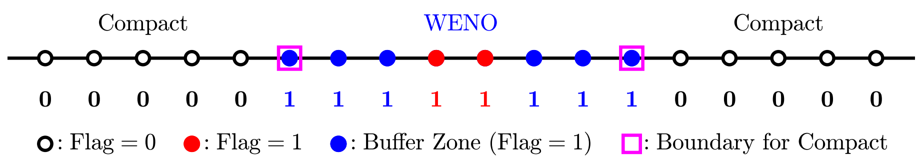

Figure 8: Diagram of the stencils for the hybrid scheme.

For simplicity, we denote the the hybrid scheme with the MR analysis, MRQ method, MRS method, C2 method and IR method as the Hybrid-MR scheme, Hybrid-MRQ scheme, Hybrid-MRS scheme, Hybrid-C2 scheme and Hybrid-IR scheme respectively. The WENO percentage is defined as the percentage of non-smooth stencils used by the fifth order WENO scheme in the whole domain. The performance of corresponding hybrid schemes are verified by simulating several classical shocked flows.

5.1 One-dimensional shock-density wave interaction problem

As a standard example in shock detection, the shock-density with Mach number 3 [14] can easily demonstrate the performance of hybrid schemes in resolving small structures and capturing small shocklet waves, as well as the ability to detect high frequency smooth

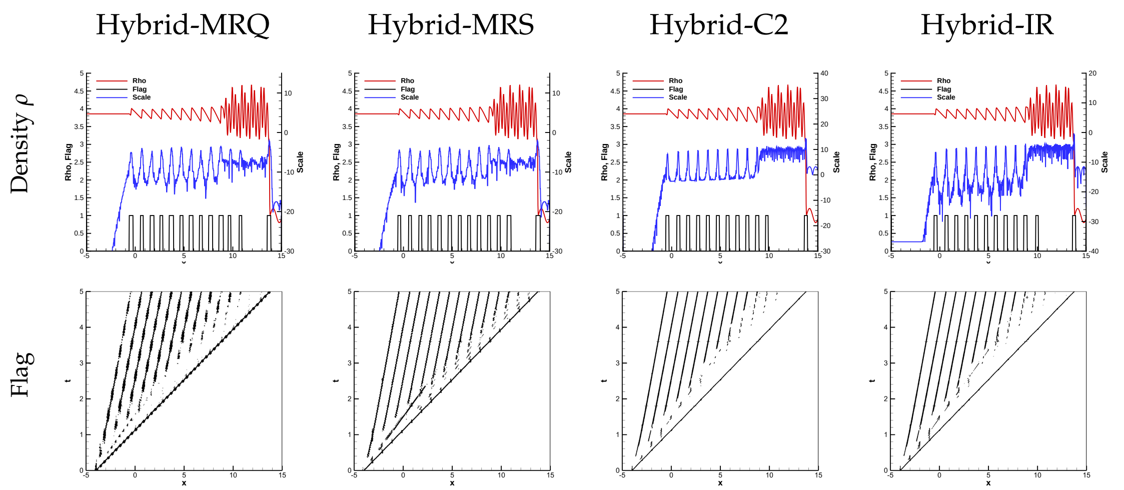

Figure 9: Shock-density wave interaction problem. The density ρ (Top) and WENO Flag (Bottom) identified by the hybrid schemes with mesh resolution $N=800$ at time $t=5$.

regions. The high frequency waves behind the main shock are smooth functions but are often misidentified as a strong gradient by a lower order shock detection algorithm [4]. The initial conditions are given by

$$(\rho,u,P)=\begin{cases} \left(\dfrac{27}{7},\dfrac{4\sqrt{35}}{9},\dfrac{31}{3}\right), & -5\leq x<-4, \\ (1+\varepsilon\sin(kx),0,1), & -4\leq x\leq 15, \end{cases}$$

where $x\in[-5,15]$, $\varepsilon=0.2$ and $k=5$.

The reflective boundary conditions are setup in this problem. In Fig. 9, it is observed that the locations of the shock are detected accurately by the four hybrid schemes with mesh resolution $N=800$. Due to the use of PauTa criterion, the Hybrid-MRS scheme, Hybrid-C2 scheme and Hybrid-IR scheme behave better than the Hybrid-MRQ scheme by identifying the shock locations with fewer grids. They not only accurately detect the big and small shocks, but also successfully identifying the high frequency waves. The CPU times and WENO percentages of the Hybrid-MRQ scheme, Hybrid-MRS scheme, Hybrid-C2 scheme and Hybrid-IR scheme are shown in Table 2. It can be seen from the results the Hybrid-C2 scheme and Hybrid-IR scheme have lower WENO percentage and are faster than Hybrid-MRQ scheme.

5.2 Two-dimensional Riemann initial value problem

According to the two-dimensional Riemann problem, 19 different initial configurations are given in literature [25], which contain rarefaction-($\overrightarrow{R}$), shock-($\overleftarrow{S}$), and contact-wave ($J^{\pm}$). The arrows ($\overrightarrow{\cdot}$) and ($\overleftarrow{\cdot}$) indicate forward and backward waves, and the superscripts $+$ and $-$ refer to negative and positive contact waves respectively. Next, we solve

Table 2: Shock-density wave interaction problem. The CPU times (in seconds) and the WENO percentage of the four hybrid schemes.

Time	Hybrid-MRQ		Hybrid-MRS		Hybrid-C2		Hybrid-IR	
	CPU	Percentage	CPU	Percentage	CPU	Percentage	CPU	percentage
$t=5.0$	1.370	23.5%	1.246	21.7%	1.227	19.7%	1.206	19.7%

the classical two-dimensional Riemann problem with initial conditions as follows:

$$\mathbf{Q}=(P,\rho,u,v)=\begin{cases} \mathbf{Q}_1=(P_1,\rho_1,u_1,v_1), & \text{if } x>x_0 \text{ and } y\geq y_0, \\ \mathbf{Q}_2=(P_2,\rho_2,u_2,v_2), & \text{if } x\leq x_0 \text{ and } y\geq y_0, \\ \mathbf{Q}_3=(P_3,\rho_3,u_3,v_3), & \text{if } x\leq x_0 \text{ and } y<y_0, \\ \mathbf{Q}_4=(P_4,\rho_4,u_4,v_4), & \text{if } x>x_0 \text{ and } y<y_0. \end{cases}$$

Considering that the calculation and shock capture results of different configurations are similar, other configurations are omitted to avoid duplicated description, and only the result of configuration 3 is presented in this paper. For configuration 3, the center (x_0,y_0) is moved from $(0.5,0.5)$ to $(0.8,0.8)$ in order to verify the performance of the hybrid scheme for long time numerical simulation and shock capturing. The configuration 3 is as follows:

- $(\overleftarrow{R_{21}},\overleftarrow{R_{32}},\overleftarrow{R_{34}},\overleftarrow{R_{41}})$, $(x_0,y_0)=(0.8,0.8)$, $t=0.8$,

$$\mathbf{Q}=\begin{cases} (1.5,1.5,0,0), \\ (0.3,0.5323,1.206,0), \\ (0.029,0.138,1.206,1.206), \\ (0.3,0.5323,0,1.206). \end{cases}$$

Fig. 10 shows the corresponding contour of density, Flag_x and Flag_y computed by the hybrid schemes. The large scale structures (including incident shock, reflected shock, Mach bar and slip plane) are consistent with those in the literature [6, 8, 25]. The corresponding Flag (black line) shows that the hybrid schemes can accurately capture the locations of discontinuities and large gradient. However, the Hybrid-MRS scheme, Hybrid-C2 scheme and Hybrid-IR scheme can detect the non-smooth regions with less grid points than the Hybrid-MRQ scheme. It results in that the Hybrid-MRQ scheme is unable to effectively depict small vortex structure.

Table 3 and Table 4 present the percentages of the WENO scheme, CPU times and speedup factors of the WENO and the four hybrid schemes for configuration 3. It can be seen from the results that the WENO percentage of Hybrid-MRS scheme, Hybrid-C2 scheme and Hybrid-IR scheme are much lower than the Hybrid-MRQ scheme. The CPU times show that three new hybrid schemes are faster than the Hybrid-MRQ scheme and about 2.8 times as fast as the WENO-Z scheme with mesh resolution $N\times M=400\times 400$.

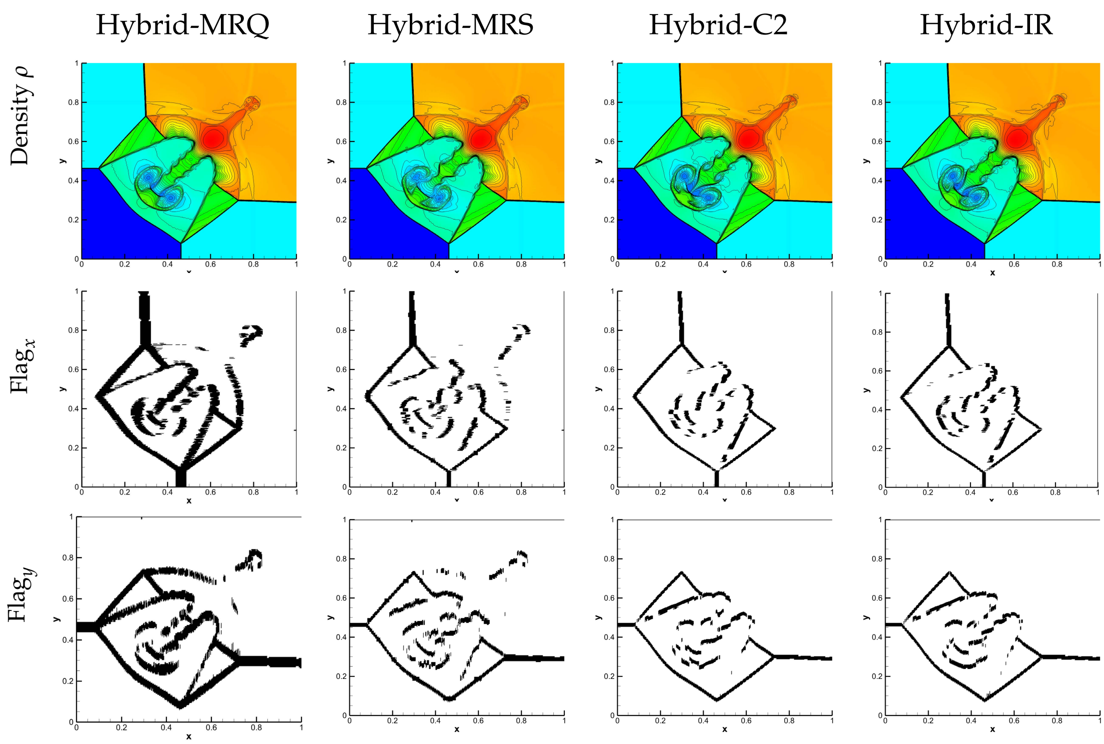

Figure 10: Riemann initial value problem. Density ρ, Flag_x and Flag_y identified by the hybrid schemes with mesh resolution $N\times M=400\times 400$ at time $t=0.25$.

5.3 Two-dimensional Mach 10 double mach reflection problem

For the two-dimensional problem, the Mach 10 double Mach reflection problem (DMR) is also considered, which can be described in detail in the article [36]. The computational region is defined as $[0,4]\times[0,1]$. The initial conditions are

$$\mathbf{Q}=(\rho,u,v,P)=\begin{cases}(8,8.25\cos\theta,-8.25\sin\theta,116.5), & x<x_0+y/\sqrt{3},\\(1.4,0,0,1), & x\geq x_0+y/\sqrt{3},\end{cases}$$

with $x_0=\frac{1}{6}$ and $\theta=\pi/6$. The final time is $t=0.2$. Supersonic inflow and free-stream outflow boundary conditions are specified at $x=0$ and $x=4$, respectively. At the lower

Table 3: Riemann initial value problem. The WENO percentage of the four hybrid schemes with different mesh resolutions.

N	Hybrid-MRQ	Hybrid-MRS	Hybrid-C2	Hybrid-IR
200×200	28.8%	16.0%	13.8%	13.8%
400×400	19.4%	11.3%	8.6%	8.7%

Table 4: Riemann initial value problem. The CPU times (in seconds) of the WENO-Z and hybrid schemes, and the speedup factors (SF) of hybrid schemes.

N	WENO-Z	Hybrid-MRQ		Hybrid-MRS		Hybrid-C2		Hybrid-IR	
	CPU	CPU	SF	CPU	SF	CPU	SF	CPU	SF
200×200	229.4	138.2	1.66	108.4	2.12	107.9	2.13	109.0	2.10
400×400	1922	831.7	2.31	699.7	2.75	690.5	2.78	684.2	2.81

boundary $y=0$, reflective boundary conditions are applied in the interval $[x_0,4]$. At the upper boundary $y=1$, the exact solution of the Mach 10 moving oblique shock is imposed.

Fig. 11 shows the density and Flag computed by the four hybrid schemes. Similar to the Hybrid-MRQ scheme, the Hybrid-MRS scheme, Hybrid-C2 scheme and Hybrid-IR scheme perform well in detecting the locations of shock waves and large gradients. The number of grid points around the locations of discontinuities and high gradient detected by the three new hybrid scheme are obviously less than that of the Hybrid-MRQ scheme. Therefore, the small structures resolved by the three new hybrid schemes are more abundant, such as the curled vortex structures in the locally enlarged density contour shown in Fig. 11.

We run the hybrid schemes with mesh resolutions 400×100 and 800×200 respectively. Table 5 and Table 6 show the percentage of WENO scheme, the CPU times along with the speedup factors of WENO-Z and hybrid schemes for solving DMR problem with different mesh resolutions. The WENO percentage of the three new hybrid schemes especially

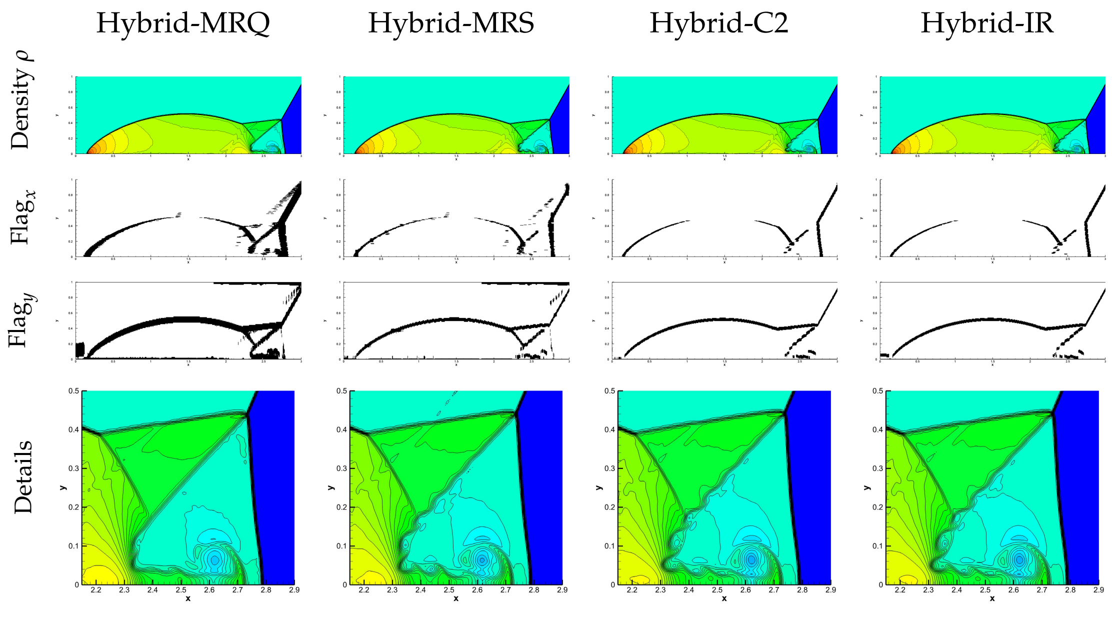

Figure 11: DMR problem. Density ρ, Flag_x and Flag_y identified by the hybrid schemes with mesh resolution $N\times M=800\times200$ at time $t=0.2$.

Table 5: DMR problem. The WENO percentage of the four hybrid schemes with different mesh resolutions.

N	Hybrid-MRQ	Hybrid-MRS	Hybrid-C2	Hybrid-IR
400×100	23.0%	14.9%	10.6%	10.5%
800×200	13.6%	8.5%	5.9%	6.0%

Table 6: DMR problem. The CPU times (in seconds) of the WENO-Z and hybrid schemes, and the speedup factors (SF) of hybrid schemes.

N	WENO-Z	Hybrid-MRQ		Hybrid-MRS		Hybrid-C2		Hybrid-IR	
	CPU	CPU	SF	CPU	SF	CPU	SF	CPU	SF
400×100	157.5	77.8	2.02	64.9	2.43	51.5	3.06	50.8	3.10
800×200	1243	496.7	2.50	432.8	2.87	426.9	2.91	421.3	2.95

Hybrid-C2 scheme and Hybrid-IR scheme are less than that of the Hybrid-MRQ scheme. Similar to the Hybrid-MRQ scheme, the three new hybrid schemes are more efficient than the WENO-Z scheme. Compared with the Hybrid-MRQ scheme, the three new hybrid schemes especially Hybrid-C2 scheme and Hybrid-IR scheme can be three times faster than the WENO-Z scheme even at a lower mesh resolution.

5.4 Two-dimensional explosion problem

The two-dimensional explosion problem is considered, which was described in detail in the article [28]. The computational region is defined as $[-3,3]\times[-3,3]$. The initial conditions include the inner and outer regions of the circle with radius $R=0.4$ centered on $(0,0)$. The initial velocities are $u=0,v=0$ and the final time is $t=3.18$, density and pressure distributions are given as follows:

$$\begin{cases} \rho(x,y)=1, \quad P(x,y)=1, & \text{if } x^2+y^2<(0.4)^2, \\ \rho(x,y)=0.125, \quad P(x,y)=0.1, & \text{otherwise.} \end{cases}$$

The boundary conditions are reflective boundary conditions and the computational region is $[0,3]\times[0,3]$. As can be seen from Fig. 12, for the explosion problem, the four hybrid schemes can find the discontinuities in oblique symmetry, but the Hybrid-MRS scheme, Hybrid-C2 scheme and Hybrid-IR scheme can identify the high-frequency smooth regions with large amplitude, so as to capture the discontinuities in the large gradient structures more accurately. The Hybrid-MRQ scheme is sensitive to small perturbations and show low efficiency. The three new hybrid schemes are insensitive to those small perturbations and can accurately capture the discontinuities in the large gradient structures. Therefore, the Hybrid-MRQ scheme is not as accurate as the three new hybrid schemes. The percentages of the WENO-Z scheme, CPU times and speedup factors of the WENO-Z and the four hybrid schemes are presented in Table 7 and Table 8. One can find that the WENO percentage of the three new hybrid schemes are much lower

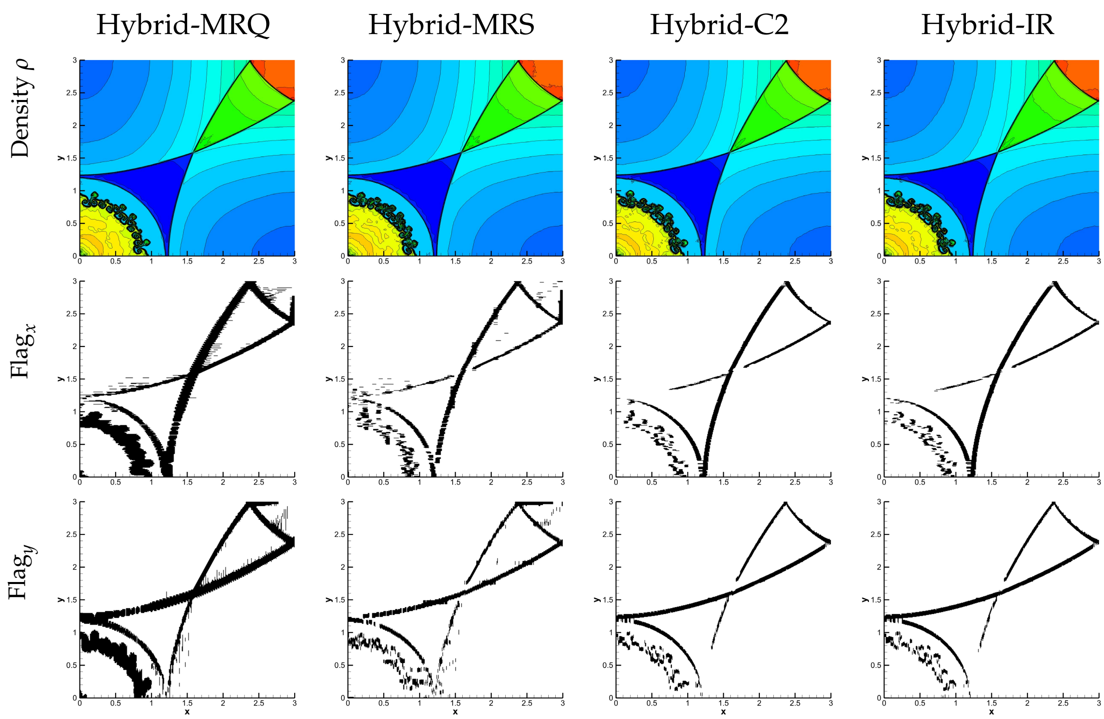

Figure 12: Explosion problem. Density ρ, Flag_x and Flag_y identified by hybrid schemes with resolution 400×400 at time $t=3.18$.

than that of the Hybrid-MRQ scheme. The CPU times show that the three new hybrid schemes, especially the Hybrid-C2 scheme and Hybrid-IR scheme, are about 3.3 times faster than the WENO-Z scheme while the Hybrid-MRQ scheme only 2.5 times with the mesh resolution $N\times M=400\times400$.

Table 7: Explosion problem. The WENO percentage of the four hybrid schemes with different mesh resolutions.

N	Hybrid-MRQ	Hybrid-MRS	Hybrid-C2	Hybrid-IR
200×200	25.2%	15.5%	13.2%	13.1%
400×400	16.4%	9.8%	7.8%	7.7%

Table 8: Explosion problem. The CPU times (in seconds) of the WENO-Z and hybrid schemes, and the speedup factors (SF) of the hybrid schemes.

N	WENO-Z	Hybrid-MRQ		Hybrid-MRS		Hybrid-C2		Hybrid-IR	
	CPU	CPU	SF	CPU	SF	CPU	SF	CPU	SF
200×200	84.3	47.4	1.78	37.6	2.24	34.4	2.45	32.6	2.59
400×400	700	271.9	2.57	226.8	3.08	208.4	3.36	199.6	3.51

5.5 Two-dimensional implosion problem

The implosion problem is one of the more challenging problems described by Liska and Wendroff [22]. The gas is in a square area $[-0.3,0.3]\times[-0.3,0.3]$. The initial density and pressure distributions are as follows:

$$(\rho,u,v,P)=\begin{cases}(0.125,0,0,0.14), & \text{if } |x-0.3|<0.15 \text{ and } |y-0.3|<0.15,\\(1,0,0,1), & \text{otherwise.}\end{cases}$$

The boundary conditions are periodic boundary conditions. The computational domain is $[0,0.6]\times[0,0.6]$ and the final time is $t=0.75$. The density with flooded contours and lines are shown in Fig. 13. Compared with the Hybrid-MRQ scheme, we observe that the WENO Flag of the three new hybrid schemes are very sharp in the x- and y-directions. Each segmented domain only contains a small number of grid points, which confirms the accuracy of the three new shock detection algorithms.

Table 9 and Table 10 present the percentages of the WENO-Z scheme, CPU times and speedup factors of the WENO-Z and the four hybrid schemes. The results show that the speeds of hybrid schemes are obviously faster than the WENO-Z scheme. The speeds of the three new hybrid schemes, especially Hybrid-C2 scheme and Hybrid-IR scheme, are faster with less WENO-Z percentage than the Hybrid-MRQ scheme.

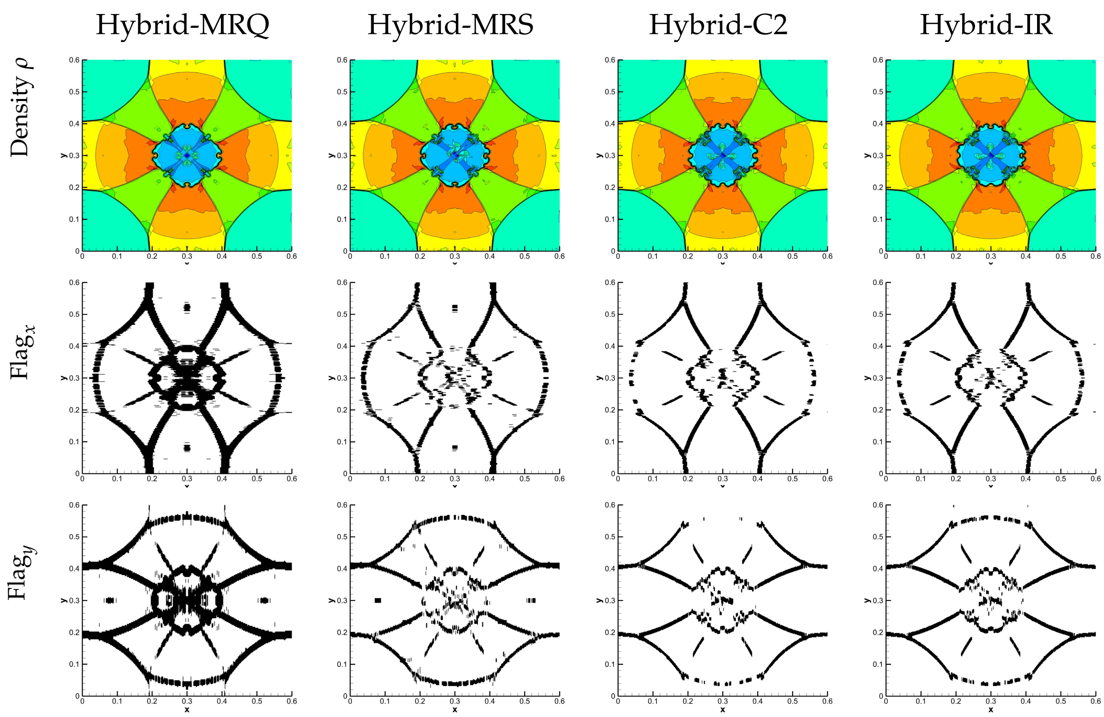

Figure 13: Implosion problem. Density ρ, Flag_x and Flag_y identified by the hybrid schemes with mesh resolution $N\times M=400\times400$ at time $t=0.75$.

Table 9: Implosion problem. The WENO percentage of the four hybrid schemes with different mesh resolutions.

N	Hybrid-MRQ	Hybrid-MRS	Hybrid-C2	Hybrid-IR
200×200	40.1%	23.0%	17.8%	18.4%
400×400	26.7%	15.7%	12.0%	13.0%

Table 10: Implosion problem. The CPU times (in seconds) of the WENO-Z and hybrid schemes, and the speedup factors (SF) of hybrid schemes.

N	WENO-Z	Hybrid-MRQ		Hybrid-MRS		Hybrid-C2		Hybrid-IR	
	CPU	CPU	SF	CPU	SF	CPU	SF	CPU	SF
200×200	134.6	97.5	1.38	71.8	1.87	68.9	1.95	67.1	2.01
400×400	1183	596.9	1.98	478.8	2.47	439.5	2.69	428.3	2.76

6 Conclusions

In this study, we replace the Tukey's boxplot method in the MR edge detector with the PauTa criterion to remove the problem-dependent parameters and improve its efficiency. Furthermore, two new edge detection approaches, which are based on second-order central difference scheme and Ren's idea, are also proposed. The accuracy, efficiency and robustness of the new edge detectors and the designed hybrid compact-WENO scheme are verified by numerous classical one- and two-dimensional examples in the image processing and compressible Euler equations with solutions containing both discontinuous and complex fine scale structures.

Appendix A: Compact finite difference schemes

The sixth-order central compact finite difference scheme [16] can be written compactly as

$$\mathbf{A}\mathbf{f}' = \mathbf{B}\mathbf{f} + \mathbf{b}, \tag{A.1}$$

where $\mathbf{A}$ and $\mathbf{B}$ are the banded coefficient matrices,

$$\mathbf{A} = \begin{pmatrix} 1 & \frac{1}{3} & & \\ \frac{1}{3} & 1 & \frac{1}{3} & \\ & \ddots & \ddots & \\ & \frac{1}{3} & \frac{1}{3} & \frac{1}{3} \\ & & \frac{1}{3} & 1 \end{pmatrix}, \tag{A.2a}$$

$$\mathbf{B}=\frac{1}{36\Delta x}\begin{pmatrix} 0 & 28 & 1 & & & \\ -28 & 0 & 28 & 1 & & \\ -1 & -28 & 0 & 28 & 1 & \\ & \ddots & \ddots & \ddots & \ddots & \ddots \\ & & -1 & -28 & 0 & 28 \\ & & & -1 & -28 & 0 \end{pmatrix}. \tag{A.2b}$$

The vector $\mathbf{b}$ is

$$\mathbf{b}=\frac{1}{36\Delta x}\left(-f_{-1}-28f_0,-f_0,0,\cdots,0,f_N,28f_N+f_{N+1}\right)^{\mathrm{T}}-\frac{1}{3}\left(f_0',0,0,\cdots,0,0,f_N'\right)^{\mathrm{T}}, \tag{A.3}$$

where $f_{-1}=f(x_0-\Delta x)$ and $f_{N+1}=f(x_N+\Delta x)$ are the ghost points.

Appendix B: Weighted essentially non-oscillatory schemes

We briefly review the fifth-order WENO-Z scheme [1]. The global stencil $S^5=(x_{i-2},\cdots,x_{i+2})$ is subdivided into three 3-point substencils $S_k=(x_{i+k-2},x_{i+k-1},x_{i+k})$, $k=0,1,2$. The fifth-order polynomial approximation $\hat{f}_{i+\frac{1}{2}}$ to the function $f(x)$ at the cell interfaces $x_{i+\frac{1}{2}}$ in the global stencil S^5 is built through the convex combination of three second-degree interpolation polynomials $\hat{f}^k(x)$ in each substencil S_k at the cell interfaces $x_{i+\frac{1}{2}}$.

$$\hat{f}_{i+\frac{1}{2}}=\sum_{k=0}^{2}\omega_k\hat{f}^k(x_{i+\frac{1}{2}}), \tag{A.4}$$

where

$$\begin{aligned}
\hat{f}^0(x_{i+\frac{1}{2}})&=\frac{1}{3}f_{i-2}-\frac{7}{6}f_{i-1}+\frac{11}{6}f_i,\\
\hat{f}^1(x_{i+\frac{1}{2}})&=-\frac{1}{6}f_{i-1}+\frac{5}{6}f_i+\frac{1}{3}f_{i+1},\\
\hat{f}^2(x_{i+\frac{1}{2}})&=\frac{1}{3}f_i+\frac{5}{6}f_{i+1}-\frac{1}{6}f_{i+2},
\end{aligned}$$

and the nonlinear weights are

$$\omega_k=\frac{\alpha_k}{\sum_{j=0}^{2}\alpha_j},\quad \alpha_k=d_k\left(1+\left(\frac{\tau_5}{\beta_k+\epsilon}\right)^p\right), \tag{A.5}$$

with the ideal weights $\{d_0=\frac{1}{10},\ d_1=\frac{3}{5},\ d_2=\frac{3}{10}\}$ and $\tau_5=|\beta_0-\beta_2|$, $\epsilon=10^{-12}$ and $p=2$ are used in this study. The smoothness indicators β_k in each substencil can be explicitly expressed as

$$\begin{aligned}
\beta_0 &= \frac{13}{12}(f_{i-2}-2f_{i-1}+f_i)^2+\frac{1}{4}(f_{i-2}-4f_{i-1}+3f_i)^2,\\
\beta_1 &= \frac{13}{12}(f_{i-1}-2f_i+f_{i+1})^2+\frac{1}{4}(f_{i-1}-f_{i+1})^2,\\
\beta_2 &= \frac{13}{12}(f_i-2f_{i+1}+f_{i+2})^2+\frac{1}{4}(3f_i-4f_{i+1}+f_{i+2})^2.
\end{aligned}$$

Acknowledgements

The author (P. Li) is partially supported by the National Natural Science Foundation of China (No. 11801383), Hebei Provincial Natural Science Foundation (No. A2020210047). Two of us (Z. Gao and C. Zhang) are partially supported by the National Natural Science Foundation of China (No. 11871443) and Shandong Provincial Qingchuang Science and Technology Project (No. 2019KJI002). The authors would like to thank the referees for the helpful suggestions.

References

[1] R. Borges, M. Carmona, B. Costa and W. S. Don, *An improved weighted essentially non-oscillatory scheme for hyperbolic conservation laws,* J. Comput. Phys., 227 (2008), pp. 3191–3211.

[2] L. L. Chen and C. Huang, *One dimensional hybrid WENO-AO method using improved troubled cell indicator based on extreme point,* Comput. Fluids, 225 (2021), 104976.

[3] B. Cockburn and C.-W. Shu, *TVB Runge-Kutta local projection discontinuous Galerkin finite element method for conservation laws II: general framework,* Math. Comput., 52 (1989), pp. 411–435.

[4] B. Costa and W. S. Don, *High order hybrid central-WENO finite difference scheme for conservation laws,* J. Comput. Appl. Math., 204(2) (2007), pp. 209–218.

[5] B. Costa and W. S. Don, *Multi-domain hybrid spectral-WENO methods for hyperbolic conservation laws,* J. Comput. Phys., 224 (2007), pp. 970–991.

[6] W. S. Don, Z. Gao, P. Li and X. Wen, *Hybrid compact-WENO finite difference scheme with conjugate Fourier shock detection algorithm for hyperbolic conservation laws,* SIAM J. Sci. Comput., 38 (2016), pp. A691–A711.

[7] L. Fu, *A hybrid method with TENO based discontinuity indicator for hyperbolic conservation laws,* Commun. Comput. Phys., 26 (2019), pp. 973–1007.

[8] Z. Gao, X. Wen and W. S. Don, *Enhanced robustness of the hybrid Compact-WENO finite difference scheme for hyperbolic conservation laws with multi-resolution analysis and Tukey's boxplot method,* J. Sci. Comput., 73 (2017), pp. 736–752.

[9] Q. Guo, D. Sun, C. Li, P. X. Liu and H. X. Zhang, *A New Discontinuity Indicator for HybridWENO Schemes,* J. Sci. Comput., 83 (2020), 28.

[10] A. Harten, *The artificial compression method for computation of shocks and contact discontinuities. III. self-adjusting hybrid schemes,* Math. Comput., 32(142) (1978), pp. 363–389.

[11] A. Harten, *High resolution schemes for hyperbolic conservation laws,* J. Comput. Phys., 49 (1983), pp. 357–393.

[12] Y. Y. HU, P. HU, W. LI AND W. H. LIAO, *A hybrid first-order and WENO scheme for the high-resolution and computationally efficient modeling of pollutant transport,* Comput. Fluids, 225 (2021), 104951.

[13] A. JAMESON, W. SCHMIDT AND E. TURKEL, *Numerical solution of the Euler equations by finite volume methods using Runge-Kutta time stepping schemes,* AIAA-1981-1259, 1981.

[14] G. S. JIANG AND C.-W. SHU, *Efficient implementation of weighted ENO Schemes,* J. Comput. Phys., 126 (1996), pp. 202–228.

[15] L. KRIVODONOVA, J. XIN, J. F. REMACLE, N. CHEVAUGEON AND J. E. FLAHERTY, *Shock detection and limiting with discontinuous Galerkin methods for hyperbolic conservation laws,* Appl. Numer. Math., 48 (2004), pp. 323–338.

[16] S. A. LELE, *Compact finite difference schemes with spectral-like resolution,* J. Comput. Phys., 103 (1992), pp. 16–42.

[17] G. LI AND J. X. QIU, *Hybrid weighted essentially non-oscillatory schemes with different indicators,* J. Comput. Phys., 229 (2010), pp. 8105–8129.

[18] G. LI, C. N. LU AND J. X. QIU, *Hybrid well-balanced WENO schemes with different indicators for shallow water equations,* J. Sci. Comput., 51 (2012), pp. 527–559.

[19] L. M. LI, Z. Z. WEN AND Z. S. WANG, *Outlier detection and correction during the process of groundwater lever monitoring base on pauta criterion with self-learning and smooth processing,* Asian Simulation Conference, (2016), pp. 497–503.

[20] P. LI, X. Q. ZHAO, Z. GAO AND B. S. WANG, *High Order hybrid weighted compact nonlinear schemes for hyperbolic conservation laws,* Adv. Appl. Math. Mech., 12 (2020), pp. 972–991.

[21] R. LI AND W. ZHONG, *An extension of the order-preserving mapping to the WENO-Z-type schemes,* Adv. Appl. Math. Mech., 15 (2023), pp. 202–243.

[22] R. LISKA AND B. WENDROFF, *Comparison of several difference schemes on 1D and 2D test problems for the Euler equations,* J. Sci. Comput., 25 (2003), pp. 995–1017.

[23] S. PIROZZOLI, *Conservative hybrid compact-WENO schemes for shock-turbulence interaction* J. Comput. Phys., 178 (2002), pp. 81–117.

[24] Y. X. REN AND H. ZHANG, *A characteristic wise hybrid compact-WENO scheme for solving hyperbolic conservation laws,* J. Comput. Phys., 192 (2003), pp. 365–386.

[25] C. W. SCHULZ-RINNE, *Classification of the Riemann problem for two-dimensional gas dynamics,* SIAM J. Math. Anal., 24 (1993), pp. 76–88.

[26] K. SHAHBAZI, J. HESTHAVEN AND X. ZHU, *Multi-dimensional hybrid Fourier continuation-WENO solvers for conservation laws,* J. Comput. Phys., 253 (2013), pp. 209–225.

[27] C.-W. SHU, *High order weighted essentially nonoscillatory schemes for convection dominated problems,* SIAM Rev., 51(1) (2009), pp. 82–126.

[28] E. F. TORO, Multidimensional Test Problems, Springer Berlin Heidelberg, (2009), pp. 585–596.

[29] J. W. TUKEY, Exploratory Data Analysis, 1st ed., Behavioral Science: Quantitative Methods, Addison-Wesley, 1977.

[30] J. R. TURNER, Standard Deviation, Encyclopedia of Behavioral Medicine, Springer, New York, 2013.

[31] U. S. VEVEK, B. ZANG AND T. H. NEW, *An efficient hybrid method for solving Euler equations,* J. Sci. Comput., 81 (2019), pp. 732–762.

[32] M. J. VUIK AND J. K. RYAN, *Automated parameters for troubled-cell indicators using outlier detection,* SIAM J. Sci. Comput., 38 (2016), pp. A84–A104.

[33] C. WANG, Y. ZHENG AND H. H. CHANG, *Does standard deviation matter? Using standard deviation to quantify security of multistage testing,* Psychometrika, 79 (2014), pp. 154–174.

[34] B.-S. WANG, W. S. DON, Z. GAO, Y. H. WANG AND X. WEN, *Hybrid compact-WENO finite difference scheme with radial basis function based shock detection method for hyperbolic conservation laws,* SIAM J. Sci. Comput., 41(6) (2018), pp. 3699–3714.

[35] P. T. WILRICH, *Robust estimates of the theoretical standard deviation to be used in interlaboratory precision experiments,* Accred. Qual. Assur., 12 (2007), pp. 231–240.

[36] P. WOODWARD AND P. COLELLA, *The numerical simulation of two dimensional fluid flow with strong shocks,* J. Comput. Phys., 54 (1984), pp. 115–173.

[37] Y. J. XU AND Z. J. CAI, *Standard deviation method for determining the weights of group multiple attribute decision making under uncertain linguistic environment,* 7th World Congress on Intelligent Control and Automation, (2008), pp. 8311–8316.

[38] Y. YANG, W. S. DON, Z. GAO AND B.-S. WANG, *Hybrid Compact-WENO Scheme with RBF-FD based discontinuity detection method for hyperbolic conservation laws,* J. Numer. Meth. Comput. Appl., 41(3) (2020), pp. 232–245.

[39] G. Y. ZHAO, M. B. SUN AND S. PIROZZOLI, *On shock sensors for hybrid compact/ WENO schemes,* Comput. Fluids., 199 (2020), 104439.

[40] X. H. ZHANG, Gaussian Distribution, C. Sammut, G. I. Webb (eds) Encyclopedia of Machine Learning, Springer, Boston, MA, 2011.

[41] Z. ZHAO, J. ZHU, Y. B. CHEN, J. X. QIU, *A new hybrid WENO scheme for hyperbolic conservation laws,* Comput. Fluids, 179 (2019), pp. 422–436.